Original Article

Can MRI accurately detect pilon articular malreduction? A quantitative comparison between CT and 3T MRI bone models

Shairah Radzi[1], Constantin Edmond Dlaska[1,2], Gary Cowin[3], Mark Robinson[4], Jit Pratap[5], Michael Andreas Schuetz[1,2], Sanjay Mishra[6], Beat Schmutz[1]

[1]Institute of Health and Biomedical Innovation, Queensland University of Technology, Brisbane, Australia; [2]Trauma Services, Princess Alexandra Hospital, Brisbane, Australia; [3]Centre of Advanced Imaging, University of Queensland, Brisbane, Australia; [4]Orthopaedics Department, Royal Brisbane and Women's Hospital, Brisbane, Australia; [5]Radiology Department, Princess Alexandra Hospital, Brisbane, Australia; [6]Department of Science & Technology, Government of India, New Delhi, India

Correspondence to: Dr. Beat Schmutz. Institute of Health and Biomedical Innovation, Queensland University of Technology, Brisbane, 60 Musk Avenue, Kelvin Grove, QLD 4059, Australia. Email: dr.beat.schmutz@gmail.com.

Background: Pilon fracture reduction is a challenging surgery. Radiographs are commonly used to assess the quality of reduction, but are limited in revealing the remaining bone incongruities. The study aimed to develop a method in quantifying articular malreductions using 3D computed tomography (CT) and magnetic resonance imaging (MRI) models.

Methods: CT and MRI data were acquired using three pairs of human cadaveric ankle specimens. Common tibial pilon fractures were simulated by performing osteotomies to the ankle specimens. Five of the created fractures [three AO type-B (43-B1), and two AO type-C (43-C1) fractures] were then reduced and stabilised using titanium implants, then rescanned. All datasets were reconstructed into CT and MRI models, and were analysed in regards to intra-articular steps and gaps, surface deviations, malrotations and maltranslations of the bone fragments.

Results: Initial results reveal that type B fracture CT and MRI models differed by ~0.2 (step), ~0.18 (surface deviations), ~0.56° (rotation) and ~0.4 mm (translation). Type C fracture MRI models showed metal artefacts extending to the articular surface, thus unsuitable for analysis. Type C fracture CT models differed from their CT and MRI contralateral models by ~0.15 (surface deviation), ~1.63° (rotation) and ~0.4 mm (translation).

Conclusions: Type B fracture MRI models were comparable to CT and may potentially be used for the postoperative assessment of articular reduction on a case-to-case basis.

Keywords: 3D; computed tomography (CT); magnetic resonance imaging (MRI); pilon; tibia; tibial plafond

Submitted Apr 27, 2016. Accepted for publication May 29, 2016.
doi: 10.21037/qims.2016.07.01
View this article at: http://dx.doi.org/10.21037/qims.2016.07.01

Introduction

Pilon fractures often require surgery to restore the displaced bone fragments back to their anatomical position. A surgeon's skill facilitates an optimal alignment, especially when re-establishing the articular surface. The quality of articular reduction is essential to restore proper function of the joint and normal range of motion. Furthermore will it avoid subsequent trauma to the neighbouring tissues and bone structure and decrease the risk of subsequent post traumatic osteo-arthritis (OA) (1-3).

A radiograph of the intact contralateral bone is routinely used to compare against the reduced fracture site to assess the quality of articular reduction post-operatively. Computed tomography (CT) will only be used when a decision needs to be made for subsequent surgical treatment (4). However, metallic implants may obscure the features of the

articular alignment (5), hence radiography may be limited in distinguishing the subchondral lines of the reduced and non-reduced individual fragments. This may also prevent clinicians from accurately assessing malalignments of the remaining fragments. The correct position of the ankle during the radiographic examination is important to avoid overlooking injuries and provide a better projection of the bone contour (6-8). Otherwise, articular incongruities may not be visualised and therefore missed, especially malrotations and maltranslations of fragments (9). This clearly suggests that other methods of articular assessment are necessary.

Although the threshold of error is restricted to 1 mm step-offs from the original anatomical position (6-8,10), the maximum allowable incongruities remains unclear because there is a lack of precise measurement tools to accurately analyse the contribution of articular incongruity and the initial trauma to the development of post-traumatic arthritis. McKinley *et al*. (2) stated that articular displacement of as small as 1 mm can alter the stress distributions of the ankle joint and potentially contribute to tissue degeneration (2), suggesting that a reliable method is critical in quantifying the threshold level for the remaining articular displacements.

Two promising imaging alternatives that can potentially overcome limitations arising from radiographs are CT and magnetic resonance imaging (MRI). CT is the gold standard in the imaging of bony structures, and have been proven to be accurate in detecting articular incongruities of the acetabulum (11). However, CT is not routinely used in pilon postoperative assessments. CT also induces higher radiation exposure and its images are more expensive compared to radiographs. MRI, however, is more popular for the diagnosis of soft tissue injuries and generates no ionising radiation (12). When fractures are accompanied by soft tissue damage, clinicians use MRI to evaluate the aspect of the overall injury (instead of both a CT and MRI).

Metallic implants generate metal artefacts on CT and MRI, which can be reduced to some extent using post-processing algorithms (13) and specific scanning protocols (14,15). A recent study by the authors quantifying metal artefacts had reported that if metal screws are ~2 or ~3 mm away from the ankle joint for CT and MRI respectively, a clear visualisation of the ankle joint can be obtained (16).

Despite their individual drawbacks, both techniques allow bones to be represented three-dimensionally (3D). Rathnayaka *et al*. (17) and Lee *et al*. (18) have used 3D bone models reconstructed from CT and MRI images to then quantified their surface differences. They reported that the mean errors between the CT and MRI models were as low as 0.23 and 0.5 mm for the human and ovine femora, respectively (17,18). These results suggested that MRI models can be reconstructed with good accuracy as compared to the CT models. The benefit of using 3D bone models has been shown in the pre-operative planning of articular fractures as the displaced fragments can be rotated and translated to move them back to their original anatomical location (19). To overcome the limitations arising from the use of radiographs, a quantitative method was developed to assess the quality of articular reduction by comparing the accuracy between CT and MRI models reconstructed from postoperative pilon images.

The purpose of this study is to determine if post-operative fracture reduction of pilon fractures can be accurately evaluated with MRI compared to CT. The goal would be to use MRI as a potential single imaging modality to quantify the accuracy of post-operative articular reduction. MRI would have the advantage to also deliver information of the soft tissue injuries and would avoid exposure of the patient to ionising radiation.

Methods

Preparation of specimens

Three pairs (left and right) of fresh frozen intact human cadaver specimens (mid shaft to foot) were acquired from the Body Bequest Program at the Medical Engineering Research Facility (MERF), Queensland University of Technology (QUT). Their age range was 70–92 years old (average: 84 years). One pair was male, and the rest female. They were kept frozen at –20 ℃ at all times except for scanning and surgical procedures.

The intact specimens were defrosted 24 hours prior to the first CT and MRI scanning to acquire intact reference imaging data. Then, five specimens were selected to simulate intra-articular fractures by creating osteotomies at the distal tibia. Out of five, three were used to create a type B fracture (AO 43-B1 fracture, pure split, partial articular), while two were used to create a type C fracture (AO 43-C1 fracture, articular simple, complete articular), as defined by the Arbeitsgemeinschaft fuer Osteosynthese (AO) Foundation (20). These two types of fractures are documented as the most common-occurring (21). The tibial plafond was exposed through a standard anteromedial or anterolateral approach, depending on the type of fracture.

After the creation of osteotomies, an open reduction and internal fixation with plate and screws was conducted.

To create a type B (AO 43-B1) fracture, a surgical saw was used to cut the medial aspect of the tibia (diaphysis), in a near sagittal plane, distally into the epiphysis, ending just proximal of the subchondral bone. Thereafter a chisel was used to create a sagittal split of the tibial plafond. The medial fragment was slightly displaced from the otherwise intact distal tibia to ensure complete bony separation and then reduced back to the tibia. Internal fixation was performed with 3.5 mm titanium medial distal tibia locking compression plates (LCP) (Synthes, Bettlach, Switzerland), and a combination of titanium non-locking (proximal) and locking (distal) cortical screws (thread Ø=3.5 mm). One specimen was reduced anatomically, while the other two were left with intra-articular step-offs of ~2 to 2.5 mm. No intra-articular gaps were created.

To create a type C (AO 43-C1) fracture, the mid-metaphysis, perpendicular to the distal articular surface, was identified with the help of K-wires. Then, the chisel was used to split the medial malleolus from the distal tibia. This resulted in a medial-lateral (ML) fracture line extending from the metaphysis to the articular surface. This process was repeated to create another fracture line in the antero-posterior (AP) direction. These specimens were reduced and internally fixed using a 3.5-mm titanium anterolateral distal tibia plate (Synthes, Bettlach, Switzerland), and a combination of titanium locking and non-locking cortical screws (thread Ø=3.5 mm).

The reduction of all specimens was confirmed using a C-arm fluoroscope.

CT and MRI data

To acquire reference CT and MRI data, all six intact specimens were CT and MRI scanned before the surgery. For CT, each specimen was positioned on the scan table by aligning the long axis of the tibia to the long axis of the CT scanner (Philips Brilliance 256-slice CT, Amsterdam, Netherlands) with scout views. The following CT protocol was used: tube voltage of 120 kVp, X-ray tube current of 190 mA, slice thickness of 0.8 mm, slice spacing of 0.4 mm, D convolution kernel, thus giving a resulting voxel size of 0.2 mm × 0.2 mm × 0.4 mm.

For MRI, each specimen was positioned on the examination bed with a spine array in place and covered with a body matrix receive coil. Following localizer images, sagittal slices were acquired by aligning the long axis of the bone to the long axis of the 3T MRI scanner (Siemens Trio, Erlangen, Germany). The following MRI parameters were used: 3D FLASH VIBE sequence, TR =11 ms, TE =1.87 ms, averages =2, flip angle =10°, pixel bandwidth =488, field-of-view (FOV) =120 mm × 140 mm, slice thickness =0.5 mm, reconstruction matrix =512×256 pixels, in-plane resolution = 0.5 mm × 0.5 mm.

After surgery, each osteotomised specimen was scanned using the same MRI parameters. As for CT, a standard clinical scan protocol was used: slice thickness of 1 mm, slice spacing of 0.5 mm, B convolution kernel, giving a resulting voxel size of 0.2 mm × 0.2 mm × 0.5 mm. This time, the iDose (low dose) function was included. High resolution CT protocols were used pre-operative so as to create geometrically accurate reference bone models (22) to be compared against bone models reconstructed using standard clinical protocols post-operative.

All CT and MRI images were saved in the DICOM (Digital Imaging and Communications in Medicine) format.

3D bone model reconstruction

All the CT and MRI data acquired were imported into the image processing software Amira 5.4.5 (FEI, Hillsboro, OR). A semi-automated threshold method developed by Rathnayaka *et al.* (23) was used to calculate the threshold values of the shaft and distal regions of the tibia, after which these values were used to segment the outer bony contours of the bone, generating 3D models from CT and MRI images. Metal artefacts found in the images were also removed by manually delineating the bone contours to exclude regions affected by these artefacts.

The 3D models were saved in STL format for importing into the reverse engineering software Rapidform 2006 (INUS Technology, Korea) for conducting the quantitative 3D assessment of the intraarticular step and gap sizes, surface deviations, as well as the bone fragment malrotations and maltranslations relative to the contralateral bone.

Intra-articular steps

The use of 3D bone models allow step and gap sizes to be measured in two ways: along the entire fracture line, and at specific points.

To measure step sizes along each fracture line, several semi-automated steps were required. Firstly, four points (P1–P4) inferior, and one point (P5) superior to the epiphyseal fragment were manually demarcated to create an

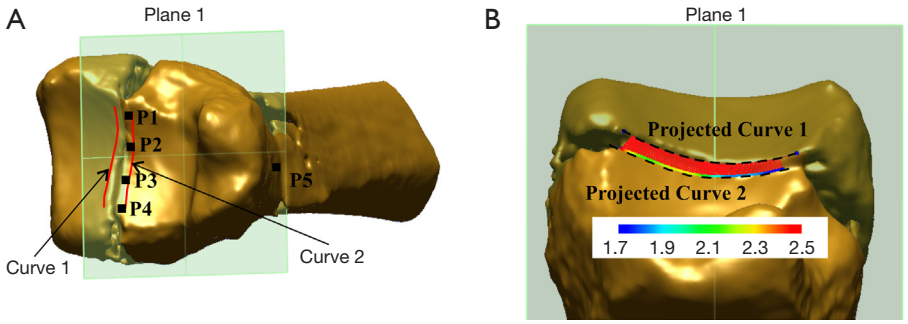

Figure 1 Measurement of intra-articular steps using curves. (A) This was done by marking points (P1–P5, black squared dots) to generate Plane 1; and drawing Curves 1 and 2 (red lines) parallel to and on opposite sides of the fracture line; (B) using the 'Curve-curve' deviation map to measure the minimum, maximum and average distances between two projected curves of interest (projected Curves 1 and 2 in dotted lines).

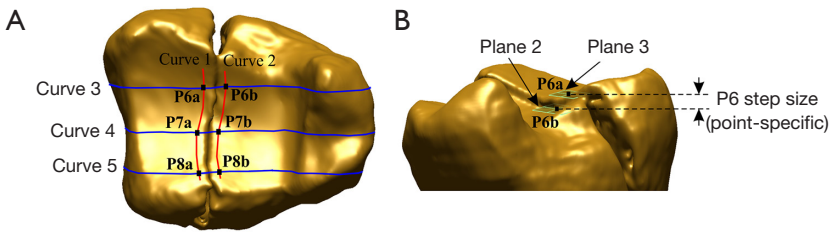

Figure 2 Measurement of intra-articular steps using paired points. (A) This was done by marking paired points (P6–P8, black squared dots) for point-specific step size measurements; (B) an example of measuring the perpendicular distance between Planes 2 and 3 relative to Point 6 (P6).

interconnecting plane parallel (Plane 1) to the fracture line. Secondly, two interpolating curves (Curves 1 and 2) were manually drawn on opposite sides of the fracture line, then perpendicularly projected onto Plane 1. These two curves were located no more than 2 mm away from the edge the fracture fragment. Finally, the two projected curves were selected and a 'Curve-curve deviation' function was used to calculate the minimum, maximum and average distance between all corresponding points along the two curves of interest (*Figure 1*).

To measure step sizes at specific points, three paired points were manually marked with the aid of Curves 1 and 2, as well as 3 perpendicular curves (Curves 3, 4 and 5) fitted to the anterior, posterior and mid-section of each fracture line. After that, a shaft axis was automatically fitted to the intact region of the mid-diaphysis, and two planes (Planes 2 and 3) were automatically fitted perpendicular to the shaft axis for each paired point (*Figure 2*). The perpendicular distances between two planes corresponding to each paired point were recorded. The maximum, minimum and average of the three distance measurements were tabulated.

Intra-articular gaps

To measure the intra-articular gap along each fracture line, several semi-automated steps were carried out. Firstly, with the aid of the 'Curvature Plot' function, intra-articular gaps in the bone surface were identified. This function shows the curvature distribution of a surface, therefore helps to identify the location of the gaps in the bone surface (*Figure 3*). Next, two interpolating curves (Curves 6 and 7) were manually drawn along the gap facing the edge of the bone fragment, and projected onto a horizontal plane (Plane 4) that was automatically fitted at 90 degrees to the shaft axis. Now with horizontal curves, the 'Curve-curve deviation' function was used to measure the minimum, maximum and average distances between the two.

For intra-articular gaps at specific points, three paired points (P9–P11) were manually demarcated inside the gap and relative to three perpendicular curves (Curves 8, 9 and 10) located at the medial, lateral and mid-section of each fracture line. Two planes (Planes 5 and 6) corresponding to each paired point and parallel to the fracture line were

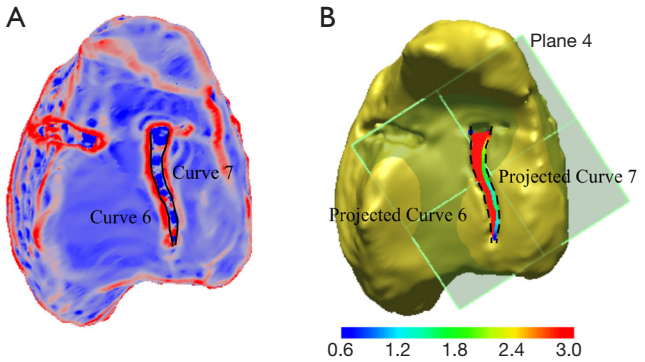

Figure 3 Measurement of intra-articular gaps using curves. (A) An example of using the 'Curvature Plot' function to identify and demarcate intra-articular gaps with curves (Curves 6 and 7 in black lines); (B) using the 'Curve-curve' deviation map to determine the maximum, minimum and average distances between two projected curves of interest (projected Curves 6 and 7 in dotted lines).

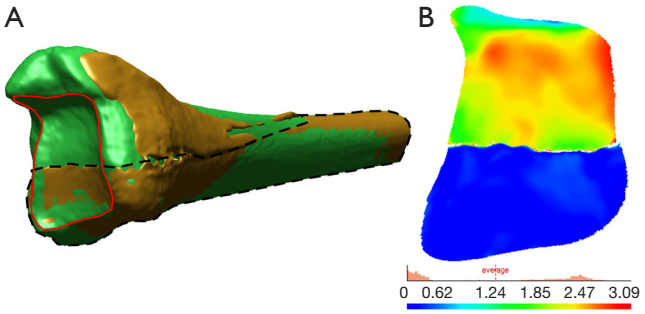

Figure 5 Measurement of surface deviation between two bone surfaces. (A) This was done in several steps, where the intact regions (black dotted lines) of the osteotomised model (brown) were initially selected for regional registration. The green model is the reference (intact, same side). The red interpolating curve was then used to cut the subchondral surface; (B) measuring the surface deviations between two selected surfaces. The regional registration process was repeated using the intact contralateral model.

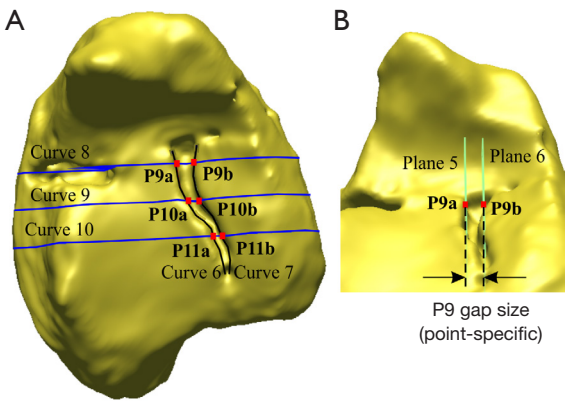

Figure 4 Measurement of intra-articular gaps using paired points. (A) This was done by marking three paired points (P9–P11, red squared dots) to measure the gap sizes of specific anatomical regions; (B) an example of measuring the horizontal distance between two planes (Planes 5 and 6) to obtain the gap size relative to Point 9 (P9).

automatically fitted. Then, the maximum, minimum and average horizontal distances from the three paired points were recorded (*Figure 4*).

Surface deviations

To quantify deviations between two surfaces, a regional registration process was conducted in Rapidform 2006. This process uses the Iterative Closest Point (ICP) algorithm to converge the distances between two similar surfaces to a minimum (24). The regional registration was conducted by selecting and aligning the intact region of the osteotomised model to the reference model. The reference model refers to the intact (same side) or contralateral bone. After completing the regional registration, the subchondral surfaces of these two models were cut using interpolating curves. Finally, a 'Shell/Shell Deviation' function was used to calculate the average and maximum surface deviations between the two selected surfaces (*Figure 5*).

To compare the accuracy between CT and MRI models, the average surface deviations between the CT and MRI models were subtracted from each other, and their differences averaged.

Malrotations

With the reference optimally aligned relative to the intact region of the osteotomised model, a coordinate system was established to determine the degree of malrotations of the displaced epiphyseal fragments relative to the reference. To minimise user-generated errors, this system was generated using the osteotomised model rather than their reference as it was a common entity for all CT and MRI models.

The coordinate system was established in several steps.

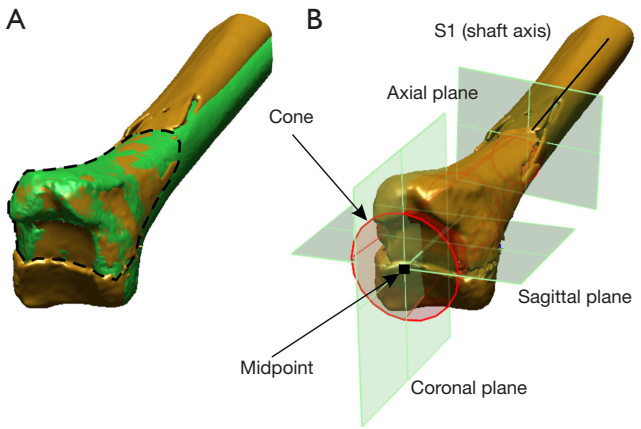

Figure 6 Establishment of the coordinate system of the osteotomised model. (A) A copy of the same system was attached to the reference (intact, same side); (B) conducting the regional registration process by selecting the displaced fragment surface (dotted lines) of the osteotomised model (brown), and aligning it with the reference (green). The regional registration process was repeated using the intact contralateral model.

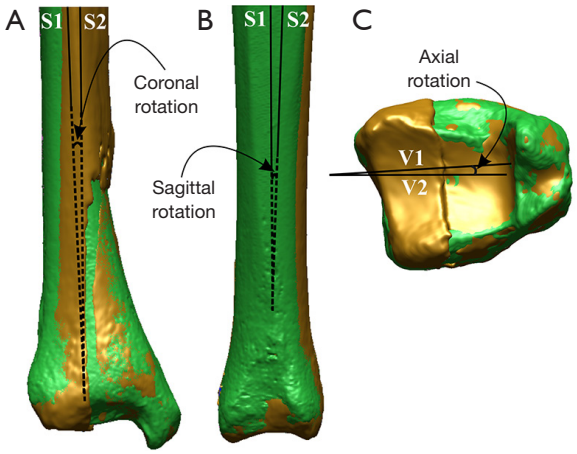

Figure 7 Using the projected vectors to measure the (A) coronal; (B) sagittal; and (C) axial malrotations relative to the coordinate system of the reference model.

Firstly, an axis was manually fitted (S1) to the intact shaft of the osteotomised model. Secondly, the distal diaphysis encompassing the bone fragment was fitted with a cone to locate the mid-point of the distal tibia. This midpoint was used to automatically generate a coronal plane in the ML direction of the distal tibia. Thirdly, using the same midpoint, a sagittal plane was created perpendicular to the coronal plane, and in the AP direction of the distal tibia. Fourthly, an axial plane was created by automatically fitting a perpendicular plane to the shaft axis. Currently, with the coordinate system of the osteotomised model established (*Figure 6*), another copy of the of the shaft axis (S2) and orthogonal planes were created and attached to the reference model.

To measure the degree of malrotations between the reference and osteotomised model, a regional registration was performed by selecting the surface of the displaced fragment and aligning this surface relative to the corresponding reference model (*Figure 6*). Using the osteotomised and the reference model's respective coordinate systems, the coronal and sagittal malrotations of the displaced fragments were measured by projecting S1 and S2 onto the coronal and sagittal planes of the reference model, and measuring the angles between these two vectors for each plane, respectively. Axial malrotations were measured by initially creating two vectors (V1 and V2) that intersect the coronal and axial planes in each coordinate system; then projecting them onto the axial plane of the reference model and measuring the angle between the two vectors (*Figure 7*).

A valgus or varus angulation of the distal part of the bone fragment was considered positive or negative with respect to the coronal and sagittal planes of the reference model. Additionally, a bone fragment that was displaced anteriorly or posteriorly relative to the axial plane was considered positive or negative, respectively.

Maltranslations

To measure the maltranslations of the displaced fragments relative to the reference, again their respective coordinate systems were used. Firstly, an intersecting point (P12) was created in the middle of the articular surface using two curves (Curves 11 and 12) that were created at the same position of the coronal and sagittal planes of the reference model. Secondly, P12 was used to measure against the coronal and sagittal planes of the osteotomised model to calculate their respective distance maltranslations (*Figure 8*).

For each quantitative method, the accuracy between the CT and MRI models were measured by calculating the malalignment of the displaced fragments. This was done by subtracting the two dimensions of interest, and reporting their absolute values, respectively.

All measurements were tested for their repeatability three times using one CT and one MRI bone model.

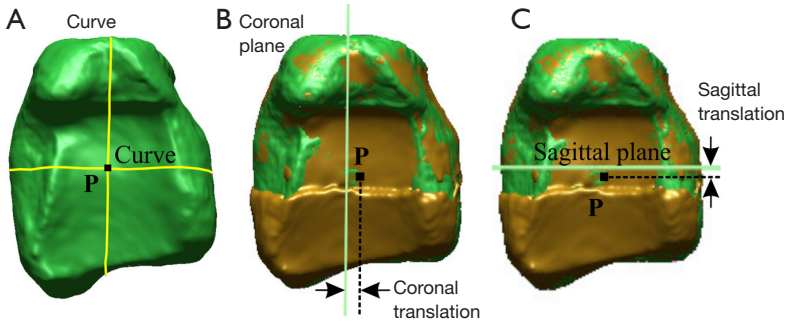

Figure 8 Measurements of translated bone fragments. (A) This is done by creating two curves (Curves 10 and 11 in yellow) from the coronal and sagittal planes attached to the reference model; and measuring the (B) coronal and (C) sagittal translations relative to the coordinate system of the osteotomised model.

Table 1 Intra-articular step size measurements of type B osteotomised specimens (mm). The fracture line extends from the medial to the lateral (ML) region of the subchondral surface

Data statistics	Curve deviation (mm)						Point-specific region (mm)					
	CT			MRI			CT			MRI		
	No. 1*	No. 2	No. 3	No. 1*	No. 2	No. 3	No. 1*	No. 2	No. 3	No. 1*	No. 2	No. 3
Min	0	1.7	2.5	0	1.0	2.4	NA	1.6	2.4	0	1.5	2.8
Max	0	2.6	3.4	0	2.5	3.2	NA	2.3	3.4	0	2.6	3.2
Ave	0	2.2	2.8	0	2.0	2.9	NA	2.0	2.9	0	2.0	3.0
SD	0	0.2	0.2	0	0.4	0.3	NA	0.4	0.5	0	0.5	0.2

*, denotes specimen with correct anatomical articular reduction. No steps and gaps were visualised from the 3D model of this specimen. CT, computed tomography; MRI, magnetic resonance imaging; SD, standard deviation.

Table 2 Intra-articular step size measurements of type C osteotomised specimens (mm). The fracture lines extend from the ML region, and anterior to posterior APregion of the subchondral surface. MRI-based models were excluded as metal artefacts obscure the intra-articular steps from being seen

Data statistics	Curve deviation (mm)				Point-specific region (mm)			
	No. 4		No. 5		No. 4		No. 5	
	AP	ML	AP	ML	AP	ML	AP	ML
Min	0	0	0.7	0.4	0	0.2	0.8	0.8
Max	1.2	0.6	2.6	2.3	0.6	0.5	1.9	1.9
Ave	0.4	0.4	1.3	1.3	0.3	0.4	1.5	1.4
SD	0.3	0.2	0.2	0.6	0.3	0.2	0.6	0.5

AP, antero-posterior; ML, medial-lateral; MRI, magnetic resonance imaging; SD, standard deviation.

Results

Step measurements of type B fracture specimens via curve deviation and point-specific methods showed differences of ≤0.7 and ≤0.4 mm between CT and MRI models (up to ±0.2 mm SD) (*Table 1*).

For type C fracture CT models, step-off differences between the curve deviation and point-specific method were ≤0.7 mm (up to ±0.6 mm SD) in either method (*Table 2*). Specimen 5 contained the largest mean step size (1.5 mm, 1.3 mm) in either method as well.

Gap measurements of type C fracture CT models

Table 3 Intra-articular gap size measurements of type C osteotomised specimens (mm). The fracture lines extend from the ML region, and AP region of the subchondral surface. Type B osteotomised specimens were excluded as no gaps were found along the subchondral surface

Data statistics	Curve deviation (mm)				Point-specific region (mm)			
	No. 4		No. 5		No. 4		No. 5	
	AP	ML	AP	ML[#]	AP	ML	AP	ML[#]
Min	0	0.7	0.1	NA	0	1.6	0.7	NA
Max	2.7	2.7	3.9	NA	1.9	2.1	3.7	NA
Ave	1.4	1.7	2.0	NA	1.0	1.9	2.4	NA
SD	0.4	0.5	1.0	NA	0.9	0.3	1.5	NA

[#], no gaps were detected for Specimen 5 in the ML direction. AP, antero-posterior; ML, medial-lateral; SD, standard deviation.

Table 4 Intra-articular surface deviation (mm) measurements to compare the differences between the reference bone model and the osteotomised bone model of interest

Fracture type	No.	CT osteotomised *vs*. CT reference (same side)			CT osteotomised *vs*. CT reference (contralateral)			CT osteotomised *vs*. MRI reference (contralateral)			MRI osteotomised *vs*. MRI reference (contralateral)		
		Max	Ave	SD	Max	Ave	SD	Max	Ave	SD	Max	Ave	SD
Type B	1*	0.47	0.15	0.12	1.30	0.40	0.33	1.35	0.44	0.37	1.45	0.42	0.32
	2	2.65	1.20	1.12	2.79	1.21	0.95	2.85	1.25	0.88	3.23	1.64	1.19
	3	2.89	1.15	1.25	3.15	1.21	0.79	2.57	1.34	0.53	2.98	1.3	1.11
Type C	4^	3.60	1.02	1.07	4.62	1.49	1.14	4.55	1.56	1.11	NA	NA	NA
	5^	3.87	1.06	0.79	4.05	1.36	1.25	3.65	1.13	0.87	NA	NA	NA

*, denotes the specimen that had correct anatomical articular reduction. ^, denotes specimens whose MRI-based models had metal artefacts extending to the subchondral surface. CT, computed tomography; MRI, magnetic resonance imaging; SD, standard deviation; NA, not applicable.

showed that the curve deviation and point-specific method differ by ≤0.8 mm (*Table 3*), with higher mean errors in the point-specific (±1.5 mm) than the curve deviation method (±1.0 mm). Specimen 5 contained the largest mean gap size (2.0 mm, 2.4 mm) for either method.

Average surface differences when comparing type B fracture CT and MRI models versus their contralateral bone were 0.18 mm (±0.22 SD). For type C fracture CT models versus their CT and MRI contralateral bone, they were 0.15 mm (±0.11 SD) (*Table 4*).

Rotational and translational differences of type B fracture CT and MRI models versus their contralateral bone were ~0.56° and ~0.4 mm, respectively. However, when comparing these against the CT reference (same side), their differences were ~2.64° and ~0.5 mm (*Table 5*). Type C fracture CT models versus MRI contralateral differed by ~1.63° and 0.4 mm (*Table 6*). Specimen 1 had the lowest degree of malrotations and maltranslations (–0.18° to –1.03°, and ~0.2 mm), while Specimen 5 had the highest (–1.55° to 10.87°, and 6.77 mm), respectively.

In terms of repeatability, CT-based models recorded a smaller degree of variability (±0.39 mm) compared to MRI-based bone models (±0.49 mm) (*Table 7*).

Discussion

Intra-articular fractures of the pilon are one of the most complex lower limb injuries. Articular reduction is commonly needed to achieve joint congruency. Radiographs are commonly used to determine the quality of reduction, but have been shown to be inaccurate and erroneous in determining the malalignments of the remaining bone fragments (5). This study proposed to develop a method for quantifying pilon reduction using 3D bone models in order to overcome limitations arising from radiographs. This was done by comparing the accuracy between MRI and CT-reconstructed 3D models from postoperative CT and MRI pilon images.

The advantage of using 3D bone models for quantifying step and gaps were that deviations can be observed across

Table 5 Rotational measurements of the displaced fragments with respect to the coronal (C), sagittal (S) and axial (A) planes of the reference coordinate system (°)

Fracture type	No.	CT osteotomised *vs*. CT reference (same side)			CT osteotomised *vs*. CT reference (contralateral)			CT osteotomised *vs*. MRI reference (contralateral)			MRI osteotomised *vs*. MRI reference (contralateral)		
		C	S	A	C	S	A	C	S	A	C	S	A
Type B	1*	–0.18	–0.17	–1.03	–0.03	–0.14	–4.23	–0.01	–0.17	–4.08	–0.25	–0.27	–3.67
	2	–1.61	–1.22	–3.27	–2.18	–0.92	–2.23	–1.63	–1.02	–1.99	–1.81	–0.99	–2.04
	3	–0.19	–0.18	–1.86	–0.78	–0.86	–0.49	–0.66	–0.9	–0.85	–0.30	–0.39	–0.6
Type C	4^	–5.80	–3.98	1.48	–5.76	–2.55	3.09	–5.37	–2.19	1.48	NA	NA	NA
	5^	–3.03	–1.55	10.87	–1.27	–1.58	9.23	–1.37	–2.07	10.86	NA	NA	NA

*, denotes the specimen that had correct anatomical articular reduction. ^, denotes specimens whose mri-based models had metal artefacts extending to the subchondral surface. CT, computed tomography; MRI, magnetic resonance imaging; NA, not applicable.

Table 6 Translational measurements of the displaced fragments with respect to the coronal (C) and sagittal (S) planes of the reference coordinate system (mm)

Fracture type	No.	CT osteotomised *vs*. CT reference (same side)		CT osteotomised *vs*. CT reference (contralateral)		CT osteotomised *vs*. MRI reference (contralateral)		MRI osteotomised *vs*. MRI reference (contralateral)	
		C	S	C	S	C	S	C	S
Type B	1*	0.2	0.2	0.7	0.3	0.7	0.4	0.6	0.4
	2	1.2	0.0	1.7	0.1	1.2	0.0	1.3	0.2
	3	0.1	0.6	0.0	0.5	0.1	0.5	0.0	0.3
Type C	4^	0.4	2.4	1.7	3.2	1.6	3.1	NA	NA
	5^	6.7	1.0	4.9	4.3	5.3	4.3	NA	NA

*, denotes the specimen that had correct anatomical articular reduction. ^, denotes specimens whose MRI-based models had metal artefacts extending to the subchondral surface. CT, computed tomography; MRI, magnetic resonance imaging; NA, not applicable.

Table 7 Repeatability test for the respective measurements

Type of measurement	Range of SD	
	CT	MRI
Intra-articular step size	0–0.19	0.05–0.49
Intra-articular gap size	0.04–0.39	NA
Intra-articular surface deviation	0.02–0.08	0.02–0.15
Rotational malalignments	0.02–0.11	0.04–0.18
Translational malalignments	0.04–0.08	0.01–0.09

CT, computed tomography; MRI, magnetic resonance imaging; SD, standard deviation; NA, not applicable.

the entire fracture line. With the curve deviations, the minimum and maximum step-offs and gaps can be located relative to the fracture line. Step and gap measurements of a particular region can also be carried out, as currently being practised in the clinic using individual CT image slices. However, it is noted that conducting point-specific measurements may not reflect the overall distance deviations across the entire fracture line. This was reflected in our results, where the distances of three-paired points from the point-specific method did not reflect the actual maximum and minimum values detected by the curve deviations. This also implies that curve deviations along fracture lines may

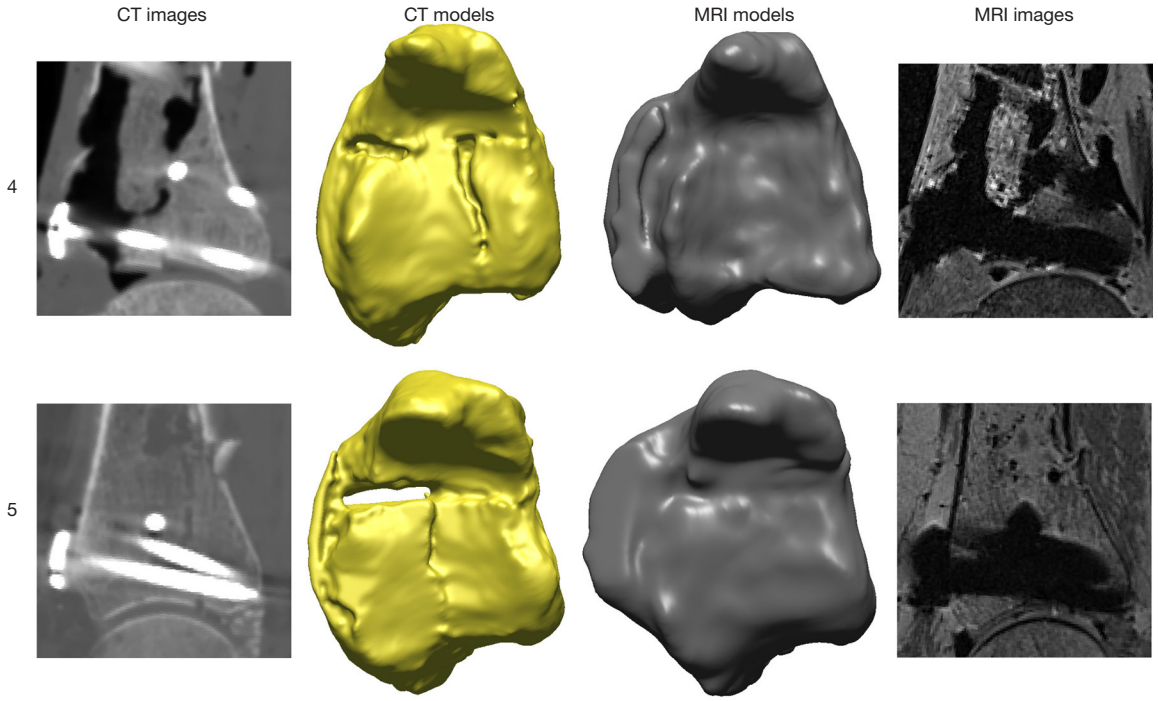

Figure 9 Subchondral surface images of type C fracture models with their corresponding sagittal CT and MRI images. CT, computed tomography; MRI, magnetic resonance imaging.

take precedence over specific points as they contain more information (minimum, maximum and average distances) for assessing the quality of reduction. Additionally, the DICOM format of the CT data can be uploaded into the 3D software. This will be useful for visually assessing and quantifying these malreductions in three orthogonal planes.

When using the intact contralateral bone to quantify measurements, the type B fracture MRI models were found to be comparable to the CT models as their differences were relatively small [0.2 mm (step), 0.18 mm (surface deviation), and 0.56° (rotation) and 0.4 mm (translation)]. These suggest that MRI and their corresponding contralateral models may be used as a template for the postoperative assessment of type B pilon fractures because they are sufficiently accurate when compared against CT.

Type C fracture MRI models were not comparable to their corresponding CT models due to the extent of metal artefacts. This may be caused by the small distance of the metal screws (≤3 mm) from the joint line (16) (*Figure 9*). Nevertheless, the CT osteotomised models were still found to be reasonably accurate when compared to their CT and MRI reference model created from the intact contralateral limb. The differences were less than 0.15 mm (average surface deviation), 1.63° (rotation) and 0.4 mm (translation). These small differences suggest that they may be used as a reference standard. In such complex cases, radiation exposure can potentially be minimised by taking MRI images of the intact opposite limb, and then comparing them with CT images of the reduced fracture site.

In Specimen 1, rotational differences of up to 3.2° (axial) were found between the contralateral and the reference bone model (same side). These differences may be caused by dissimilarities in the surface geometry between the left and right bones due to visible signs of osteophyte formation from an aged volunteer, unlike another study that used healthy specimens (25). Specimen 5, however, contained the highest malalignments (rotation: 10.87°; surface deviation: 3.87 mm and translation: 6.7 mm). Based on these values, it appears to demonstrate that these measurements reflect the quality of the articular reduction (*Figure 10*), such that larger measurements will show a poorer quality of reduction. However, based on clinical criteria stating that the varus/valgus angle should not exceed 5° (26), and that the malrotations should not exceed 10° when compared to the intact contralateral bone (27-29) in order to obtain an acceptable quality of reduction, the rotational

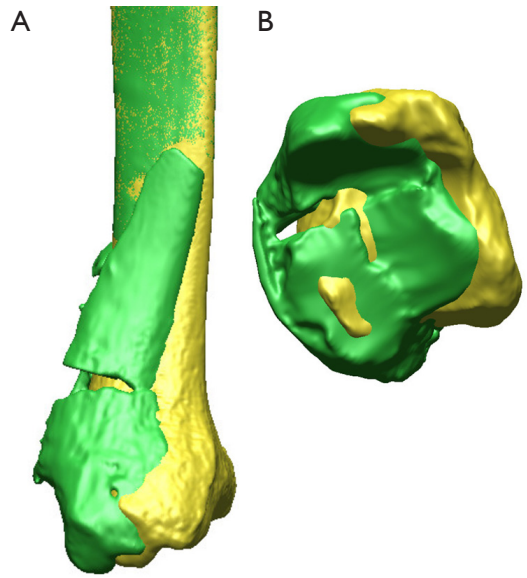

Figure 10 Malreduction of Specimen 5 (in green) relative to the reference (intact, same side) model (in yellow) in the (A) sagittal; and (B) axial views.

measurements were well within these tolerance levels, with one borderline case from Specimen 5 (10.87°). Then again, using 3D models, borderline cases may be identified with increased accuracy, especially in complex fractures as they are more challenging to achieve anatomical reduction. In any case, since the contralateral bone is routinely used for the postoperative assessment of pilon fractures, it is recommended to consider such differences when quantifying bone reduction, particularly for aged patients.

There appears to be a correlation between the maximum surface deviations and the sagittal malrotations when comparing the osteotomised versus the intact contralateral model for all the specimens. The colour codes in the map (*Figure 5*) indicate that if the region is highlighted in red, the deviation between two surfaces is maximum compared to regions in blue, and therefore may reflect the extent of malrotations. This was similarly seen when comparing the step and gap sizes versus the maltranslations for the type C osteotomised specimens. These findings appear to suggest that the degree of malrotations and maltranslations is reflected in the surface deviations, step and gap size measurements. Consequently, to obtain a detailed assessment pertaining to the quality of reduction, a minimum of three quantification methods is suggested, which are the step and gap sizes, and the surface deviation measurements. However, it is acknowledged that the distance measurements may not contain information regarding the degree of malrotations in the three anatomical planes. As such, angular measurements may be included to enhance the accuracy of the quantitative analysis. A larger sample size can potentially support these observations.

Nevertheless, it is easier to visualise the overall quality of bone reduction using 3D models versus radiographs and individual CT and MRI image slices, because the surface deviation maps are able to reveal the distance between two surfaces using colour codes. This method cannot be visualised on a two-dimensional radiograph. However, it is noted that while 3D models provide more information for assessing the quality of bone reduction, the model-reconstruction process is time-consuming, especially with the presence of metal artefacts. Therefore, an automated method will help expedite this process and can form part of future work.

Errors may come from the segmentation process. While the Canny-edge detection filter algorithm was to outline the cortical boundaries of the diaphyseal regions of the bone (23), and was reported to generate a mean error of ~0.23 mm between CT versus MRI-based bone models (17), manual segmentation was still required to delineate the bony edges in the epiphyseal regions due to the existence of metal artefacts. Osteophytes were also found in two specimens. A manual removal of these two entities may contribute user-generated errors. Additionally, the voxel sizes were different when acquiring the CT images before and after surgery, and versus the MRI images, which may also contribute to inaccuracies. The purpose of acquiring CT reference data of a higher resolution was to compare these with the CT protocols routinely used in the clinic for generating postoperative data. In spite of these errors, the mean surface difference between CT and MRI was ~0.18 mm, thus reasonably small and would not have adversely affected the outcome of the study. These results were also consistent with those of Lee *et al.* [2008], who investigated the accuracy between CT and MRI-based femoral models (0.5±0.3 mm).

Errors may also come from manually picking points to create the planes parallel and perpendicular to the fracture lines for measuring the intra-articular steps and gaps. This was reflected in the repeatability test showing higher mean errors (0.39 and 0.49 mm respectively) as compared to other types of measurements. However, these values were still smaller than the highest intra-articular step (±0.6 mm) and gap (±0.9 mm) mean errors. Again, this suggests that the quantitative method developed may hold sufficient accuracy

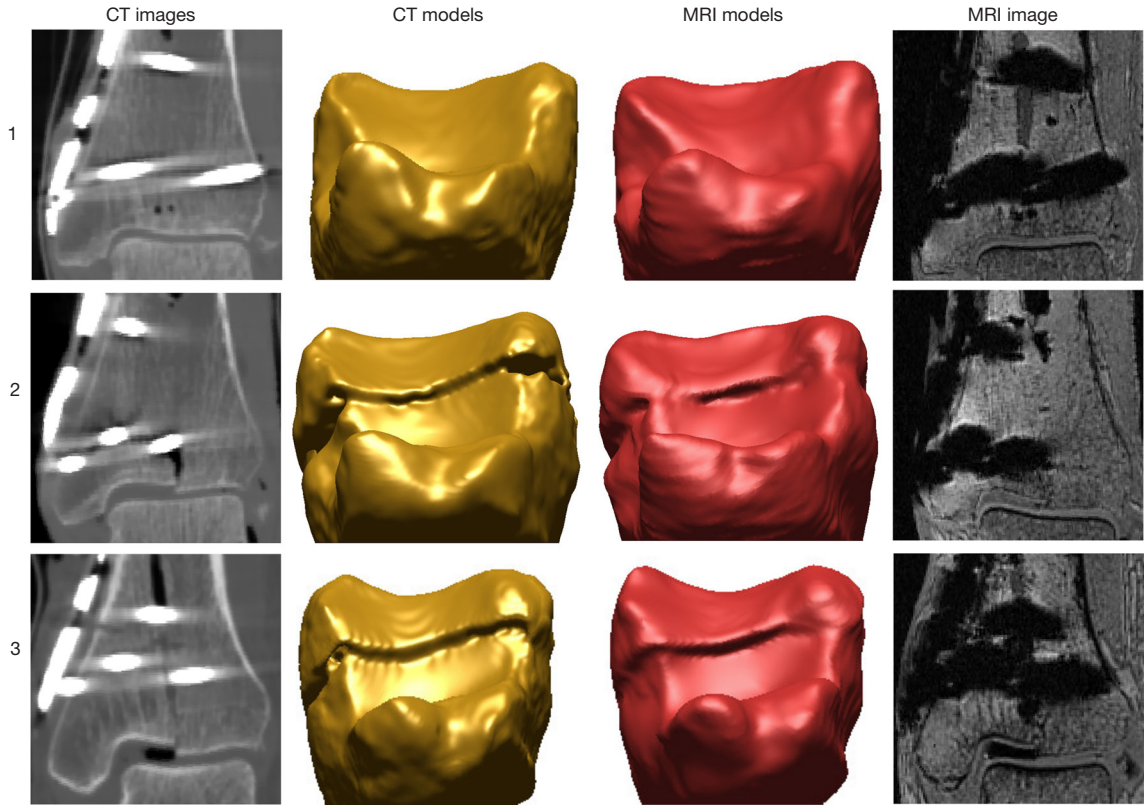

Figure 11 Subchondral surface images of type B fracture models with their corresponding coronal CT and MRI images. CT, computed tomography; MRI, magnetic resonance imaging.

in analysing the extent of step-offs and gaps.

A radiograph's technical limitation is that fracture lines cannot be visualised in the axial plane. Even with the coronal and sagittal projections, metal implants may obstruct the articular surface, and may cause measurement inaccuracies if the X-rays are over-projected. From the reported results, it is found that there is potential for MRI models to be used for quantifying the mal-alignments of type B fractures since the metal artefacts did not extend to the articular surface. This is likely because the metal screws were more than 3 mm away from the joint (16). As these fractures were simple, it was also easier to identify the fractures lines, unlike type C fractures. By taking into account the fracture type and screw distance to the joint line, MRI may be a suitable postoperative imaging alternative to CT for pilon fractures. Moreover, MRI can help avoid exposing patients to unnecessary ionising radiation.

Intra-articular gap size measurements were excluded in all six type B fracture CT and MRI models. Of these six, the CT and MRI models from Specimen 1 had a correct anatomical articular reduction, therefore step-offs and gaps were not present (*Figure 11*). Additionally, two type C fracture MRI models were excluded as the metal artefacts extended to the articular surface and could not be fully removed, therefore malalignment of the displaced fragments were left undetected (*Figure 9*).

This study's limitations include the small number of osteotomised specimens (n=5). Therefore, statistical analysis was not conducted to determine the statistical significance between CT and MRI models as the initial results would not have represented the general population. This study may extend to include to a larger number of specimens to make a definitive conclusion. Advanced metal artefact reduction (MAR) protocols such as multispectral imaging and ultrashort echo-time sequences (30) were also not included as it was intended to use clinically available protocols widely used in the current medical practices. Nevertheless, it is agreed that such sequences may help to reduce metal artefact size in MRI images to a larger extent (14,15). It was also noted that a recent study had investigated using the Ultra-

High Field (UHF) 7 Tesla scanner for providing a higher image quality of the ankle (31). As such, the potential of increasing the accuracy in reconstructing the bone models with 7T postoperative images can be examined in the future.

Conclusions

MRI models (type B fracture) can potentially be used for the quantification of pilon articular malreduction as initial results showed that they are comparable to the CT models. MRI models, however, were found to be more suitable for simple fractures, whereas CT models may be used for both simple and complex fractures. The fracture complexity, screw distance to the joint line, and implant material, type and size needs to be considered for the possibility of using MRI for a clear visualisation of the articular surface. Radiation may also be minimised by comparing MRI contralateral bone images to a CT image of the fractured side. For a comprehensive assessment on the quality of joint reduction, at least three types of measurement methods: step and gap sizes, as well as surface deviation measurements of 3D models, are recommended.

Acknowledgements

Assisted by Mr. Ian Mellor for the handling of the cadaver specimens. C-arm fluoroscope operated by Mr. Kimble Dunster during surgery. Subsidised by the National Imaging Facility, University of Queensland (Brisbane, Australia).

Footnote

Conflicts of Interest: Dr. Schmutz has received an industrial scholarship from Synthes GmBH. The other authors have no conflicts of interest to declare.

Ethical Statement: This study was approved (Approval No: 1200000134) by the University Human Research Ethics Committee of Queensland University of Technology (QUT) and used donor specimens from the body bequest program at QUT's Medical Engineering Research Facility (MERF). Body donors or their authorised next of kin have given written informed consent for use of these specimen in medical research.

References

1. Thomas TP, Anderson DD, Willis AR, Liu P, Frank MC, Marsh JL, Brown TD. A computational/experimental platform for investigating three-dimensional puzzle solving of comminuted articular fractures. Comput Methods Biomech Biomed Engin 2011;14:263-70.
2. McKinley TO, Rudert MJ, Tochigi Y, Pedersen DR, Koos DC, Baer TE, Brown TD. Incongruity-dependent changes of contact stress rates in human cadaveric ankles. J Orthop Trauma 2006;20:732-8.
3. Borrelli J Jr, Ricci WM, Steger-May K, Totty WG, Goldfarb C. Postoperative radiographic assessment of acetabular fractures: a comparison of plain radiographs and CT scans. J Orthop Trauma 2005;19:299-304.
4. Lesic A. Bumbasirevic M. Ankle fractures. Current Orthopaedics 2004;18:232-44.
5. Pollak AN, McCarthy ML, Bess RS, Agel J, Swiontkowski MF. Outcomes after treatment of high-energy tibial plafond fractures. J Bone Joint Surg Am 2003;85-A:1893-900.
6. Dietrich A, Lill H, Engel T, Schönfelder M, Josten C. Conservative functional treatment of ankle fractures. Arch Orthop Trauma Surg 2002;122:165-8.
7. Tarkin IS, Clare MP, Marcantonio A, Pape HC. An update on the management of high-energy pilon fractures. Injury 2008;39:142-54.
8. Joveniaux P, Ohl X, Harisboure A, Berrichi A, Labatut L, Simon P, Mainard D, Vix N, Dehoux E. Distal tibia fractures: management and complications of 101 cases. Int Orthop 2010;34:583-8.
9. Graves ML, Kosko J, Barei DP, Taitsman LA, Tarquinio TA, Russell GV, Woodall J Jr, Porter SE. Lateral ankle radiographs: do we really understand what we are seeing? J Orthop Trauma 2011;25:106-9.
10. Sommer C, Rüedi TP. Tibia distal (pilon). In: Rüedi TP, Murphy WM. editors. AO Principles of Fracture Management. New York, NY: Thieme, 2000:543-60.
11. Moed BR, Carr SE, Gruson KI, Watson JT, Craig JG. Computed tomographic assessment of fractures of the posterior wall of the acetabulum after operative treatment. J Bone Joint Surg Am 2003;85-A:512-22.
12. Muhammad A, Tim S, Crues III J. MRI of the ankle. Applied Radiology 2006;35:27-39.
13. Naranjo V, Lloréns R, Alcañiz M, López-Mir F. Metal artifact reduction in dental CT images using polar mathematical morphology. Comput Methods Programs Biomed 2011;102:64-74.
14. Koch KM, Brau AC, Chen W, Gold GE, Hargreaves BA, Koff M, McKinnon GC, Potter HG, King KF. Imaging near metal with a MAVRIC-SEMAC hybrid. Magn Reson

Med 2011;65:71-82.
15. Lu W, Pauly KB, Gold GE, Pauly JM, Hargreaves BA. SEMAC: Slice Encoding for Metal Artifact Correction in MRI. Magn Reson Med 2009;62:66-76.
16. Radzi S, Cowin G, Robinson M, Pratap J, Volp A, Schuetz MA, Schmutz B. Metal artifacts from titanium and steel screws in CT, 1.5T and 3T MR images of the tibial Pilon: a quantitative assessment in 3D. Quant Imaging Med Surg 2014;4:163-72.
17. Rathnayaka K, Momot KI, Noser H, Volp A, Schuetz MA, Sahama T, Schmutz B. Quantification of the accuracy of MRI generated 3D models of long bones compared to CT generated 3D models. Med Eng Phys 2012;34:357-63.
18. Lee YS, Seon JK, Shin VI, Kim GH, Jeon M. Anatomical evaluation of CT-MRI combined femoral model. Biomed Eng Online 2008;7:6.
19. Thomas TP, Anderson DD, Willis AR, Liu P, Marsh JL, Brown TD. ASB Clinical Biomechanics Award Paper 2010 Virtual pre-operative reconstruction planning for comminuted articular fractures. Clin Biomech (Bristol, Avon) 2011;26:109-15.
20. Hessmann M, Nork S, Sommer C, Twaddle B. Distal tibia: AO Foundation; 2008 [4/5/2014]. Available online: https://www2.aofoundation.org/wps/portal/surgery?showPage=diagnosis&bone=Tibia&segment=Distal
21. Topliss CJ, Jackson M, Atkins RM. Anatomy of pilon fractures of the distal tibia. J Bone Joint Surg Br 2005;87:692-7.
22. Schmutz B, Wullschleger ME, Schuetz MA. editors. The effect of CT slice spacing on the geometry of 3D models. Proceedings 6th Australasian Biomechanics Conference (2007); The University of Auckland, New Zealand.
23. Rathnayaka K, Sahama T, Schuetz MA, Schmutz B. Effects of CT image segmentation methods on the accuracy of long bone 3D reconstructions. Med Eng Phys 2011;33:226-33.
24. Besl PJ, McKay ND. A Method for registration of 3-D shapes. IEEE Trans Pattern Anal Mach Intell 1992;14:239-56.
25. Radzi S, Uesugi M, Baird A, Mishra S, Schuetz M, Schmutz B. Assessing the bilateral geometrical differences of the tibia : are they the same? Medical Engineering and Physics 2014;36:1618-25.
26. Ruedi TP, Murphy WM. AO Principles of Fracture Management. New York: Thieme Stuttgart, 2001.
27. McKee MD, Schemitsch EH, Waddell JP, Yoo D. A prospective, randomized clinical trial comparing tibial nailing using fracture table traction versus manual traction. J Orthop Trauma 1999;13:463-9.
28. Puloski S, Romano C, Buckley R, Powell J. Rotational malalignment of the tibia following reamed intramedullary nail fixation. J Orthop Trauma 2004;18:397-402.
29. Wiss DA, Stetson WB. Unstable fractures of the tibia treated with a reamed intramedullary interlocking nail. Clin Orthop Relat Res 1995;(315):56-63.
30. Hargreaves BA, Worters PW, Pauly KB, Pauly JM, Koch KM, Gold GE. Metal-induced artifacts in MRI. AJR Am J Roentgenol 2011;197:547-55.
31. Juras V, Welsch G, Bär P, Kronnerwetter C, Fujita H, Trattnig S. Comparison of 3T and 7T MRI clinical sequences for ankle imaging. Eur J Radiol 2012;81:1846-50.

Cite this article as: Radzi S, Dlaska CE, Cowin G, Robinson M, Pratap J, Schuetz MA, Mishra S, Schmutz B. Can MRI accurately detect pilon articular malreduction? A quantitative comparison between CT and 3T MRI bone models. Quant Imaging Med Surg 2016;6(6):634-647. doi: 10.21037/qims.2016.07.01

